

Spectroscopic verification of very luminous galaxy candidates in the early universe

Pablo Arrabal Haro^{1*}, Mark Dickinson¹, Steven L. Finkelstein², Jeyhan S. Kartaltepe³, Callum T. Donnan⁴, Denis Burgarella⁵, Adam C. Carnall⁴, Fergus Cullen⁴, James S. Dunlop⁴, Vital Fernández⁶, Seiji Fujimoto^{7,8}, Intae Jung⁹, Melanie Krips¹⁰, Rebecca L. Larson^{2,11}, Casey Papovich^{12,13}, Pablo G. Pérez-González¹⁴, Ricardo O. Amorín^{6,15}, Micaela B. Bagley², Véronique Buat⁵, Caitlin M. Casey², Katherine Chworowsky^{2,11}, Seth H. Cohen¹⁶, Henry C. Ferguson⁹, Mauro Giavalisco¹⁷, Marc Huertas-Company^{18,19,20}, Taylor A. Hutchison^{21,22}, Dale D. Kocevski²³, Anton M. Koekemoer⁹, Ray A. Lucas⁹, Derek J. McLeod⁴, Ross J. McLure⁴, Norbert Pirzkal⁹, Jonathan R. Trump²⁴, Benjamin J. Weiner²⁵, Stephen M. Wilkins^{26,27} and Jorge A. Zavala²⁸

¹NSF's National Optical-Infrared Astronomy Research Laboratory, 950 N. Cherry Ave., Tucson, AZ 85719, USA.

²Department of Astronomy, The University of Texas at Austin, Austin, TX, USA.

³Laboratory for Multiwavelength Astrophysics, School of Physics and Astronomy, Rochester Institute of Technology, 84 Lomb Memorial Drive, Rochester, NY 14623, USA.

⁴Institute for Astronomy, University of Edinburgh, Royal Observatory, Edinburgh EH9 3HJ, UK.

⁵Aix Marseille Univ, CNRS, CNES, LAM Marseille, France.

⁶Instituto de Investigación Multidisciplinar en Ciencia y Tecnología, Universidad de La Serena, Raul Bitrán 1305, La Serena 2204000, Chile.

⁷Cosmic Dawn Center (DAWN), Jagtvej 128, DK2200 Copenhagen N, Denmark.

- ⁸Niels Bohr Institute, University of Copenhagen, Lyngbyvej 2, DK2100 Copenhagen Ø, Denmark.
- ⁹Space Telescope Science Institute, Baltimore, MD, 21218, USA.
- ¹⁰IRAM, Domaine Universitaire, 300 rue de la Piscine, 38406 Saint-Martin-d'Hères, France.
- ¹¹NSF Graduate Fellow.
- ¹²Department of Physics and Astronomy, Texas A&M University, College Station, TX, 77843-4242 USA.
- ¹³George P. and Cynthia Woods Mitchell Institute for Fundamental Physics and Astronomy, Texas A&M University, College Station, TX, 77843-4242 USA.
- ¹⁴Centro de Astrobiología (CAB), CSIC-INTA, Ctra. de Ajalvir km 4, Torrejón de Ardoz, E-28850, Madrid, Spain.
- ¹⁵Departamento de Astronomía, Universidad de La Serena, Av. Juan Cisternas 1200 Norte, La Serena 1720236, Chile.
- ¹⁶School of Earth and Space Exploration, Arizona State University, Tempe, AZ, 85287 USA.
- ¹⁷University of Massachusetts Amherst, 710 North Pleasant Street, Amherst, MA 01003-9305, USA.
- ¹⁸Instituto de Astrofísica de Canarias, La Laguna, Tenerife, Spain.
- ¹⁹Universidad de la Laguna, La Laguna, Tenerife, Spain.
- ²⁰Université Paris-Cité, LERMA - Observatoire de Paris, PSL, Paris, France.
- ²¹Astrophysics Science Division, NASA Goddard Space Flight Center, 8800 Greenbelt Rd, Greenbelt, MD 20771, USA.
- ²²NASA Postdoctoral Fellow.
- ²³Department of Physics and Astronomy, Colby College, Waterville, ME 04901, USA.
- ²⁴Department of Physics, 196 Auditorium Road, Unit 3046, University of Connecticut, Storrs, CT 06269, USA.
- ²⁵MMT/Steward Observatory, University of Arizona, 933 N. Cherry Ave., Tucson, AZ 85721, USA.
- ²⁶Astronomy Centre, University of Sussex, Falmer, Brighton BN1 9QH, UK.
- ²⁷Institute of Space Sciences and Astronomy, University of Malta, Msida MSD 2080, Malta.
- ²⁸National Astronomical Observatory of Japan, 2-21-1 Osawa, Mitaka, Tokyo 181-8588, Japan.

*Corresponding author(s). E-mail(s): parrabalh@gmail.com;

During the first 500 million years of cosmic history, the first stars and galaxies formed and seeded the cosmos with heavy elements [e.g., 1–4]. These early galaxies illuminated the transition from the cosmic “dark ages” to the reionization of the intergalactic medium. This transitional period has been largely inaccessible to direct observation until the recent commissioning of *JWST*, which has extended our observational reach into that epoch. Excitingly, the first *JWST* science observations uncovered a surprisingly high abundance of early star-forming galaxies [e.g., 5–12]. However, the distances (redshifts) of these galaxies were, by necessity, estimated from multi-band photometry. Photometric redshifts, while generally robust, can suffer from uncertainties and/or degeneracies. Spectroscopic measurements of the precise redshifts are required to validate these sources and to reliably quantify their space densities, stellar masses, and star formation rates, which provide powerful constraints on galaxy formation models and cosmology [13]. Here we present the results of *JWST* follow-up spectroscopy of a small sample of galaxies suspected to be amongst the most distant yet observed. We confirm redshifts $z > 10$ for two galaxies, including one of the first bright *JWST*-discovered candidates with $z = 11.4$, and show that another galaxy with suggested $z \approx 16$ instead has $z = 4.9$, with strong emission lines that mimic the expected colors of more distant objects. These results reinforce the evidence for the rapid production of luminous galaxies in the very young Universe, while also highlighting the necessity of spectroscopic verification for remarkable candidates.

The spectroscopic targets were selected from *JWST*/NIRCam [14–16] imaging obtained through the Cosmic Evolution Early Release Science (CEERS) Survey [17] because their colors at wavelengths of 1 – 5 microns matched predictions for galaxies with redshifts $z > 9$ [12], including the key signature of a “break” in flux density at wavelengths shorter than that of redshifted hydrogen Lyman α ($\text{Ly}\alpha$; rest-frame wavelength $\lambda_{\text{rest}} = 1216\text{\AA}$) due to the largely-neutral intergalactic medium (IGM) expected at early times. Here we focus attention on two bright extreme-redshift candidates, one with a photometric redshift $z \simeq 11.1$ (J141946.36+525632.8, aka Maisie’s Galaxy [7], here MSA ID 1; see Methods for updated photometric redshift measurement) and another with a photometric redshift $z \simeq 16.4$ (CEERS-93316 [8]; here MSA ID 0). At their estimated redshifts, these two galaxies would have UV luminosities $\simeq 4$ and $\simeq 15$ times brighter than the most distant spectroscopically confirmed galaxy to date ($z = 13.2$ [18]). We show these photometric redshift estimates in Figure 1.

Although independent analyses by different teams [7, 8, 12, 19] identified these two candidates using 7-band *JWST*/NIRCam photometry, it is possible for foreground objects to infiltrate high-redshift samples due to unusual colors resulting from older stellar populations, strong nebular emission lines, and/or dust reddening [8, 20, 21]. A tentative detection at $850\ \mu\text{m}$ of dust

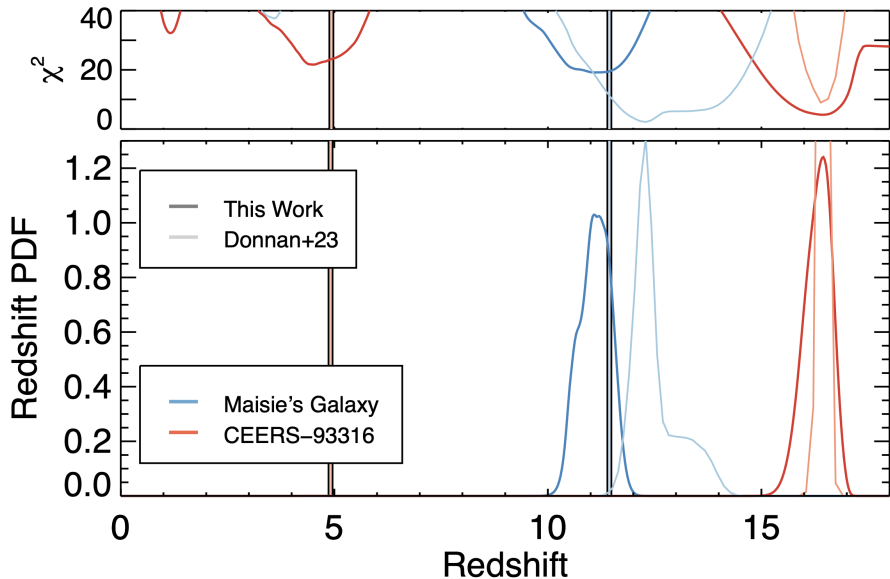


Fig. 1 The likelihood (bottom) and χ^2 goodness-of-fit (top) distribution functions for the photometric redshift, derived from the *JWST* CEERS photometry. Results for Maisie’s Galaxy [7, 12] are in blue, and the $z \sim 16.5$ candidate galaxy discovered by [8] are in red. The line shading denotes the results using the photometric measurements from each team. The results between the two methods are broadly similar, though our use of *HST* photometry (see Methods) results in a redshift closer to the spectroscopic value due to a weak detection in the *HST*/WFC3 $1\ \mu\text{m}$ band. The spectroscopic measurements of $z = 11.44$ and $z = 4.912$ from this paper are shown by the thick vertical lines.

emission in the vicinity of CEERS-93316 [22] could support the dust reddening hypothesis, but we have investigated this using new observations at 1.1 mm with the NOEMA interferometer and localized the dust emission to another galaxy approximately 1.5 arcsec away (see Methods for details). Nonetheless, reddening could still affect the observed colors of CEERS-93316.

We observed both galaxies with *JWST*/NIRSpec [23] using its multi-object spectroscopy mode and prism disperser, whose low spectral resolution at wavelengths shorter than $2.5\ \mu\text{m}$ affords high sensitivity for detecting faint continuum emission and spectral breaks. Details of the observations and data analysis, as well as results from simultaneous observations of several other candidate $z > 9$ galaxies, are summarized in the Methods section.

The spectrum of Maisie’s Galaxy (Figure 2) shows well-detected continuum emission with a sharp break, below which no significant flux is detected. The most likely interpretations of this feature are the Ly α IGM break ($\lambda_{\text{rest}} = 1216\text{\AA}$) or the Balmer break ($\lambda_{\text{rest}} = 3646\text{\AA}$); the latter is prominent in galaxies where star formation ceased more than 100 Myr before the time of observation. Integrating the spectra in wavelength intervals redder and bluer than the observed breaks, we measure a 3σ limit on the flux density ratio > 2.6 , inconsistent with values expected for Balmer breaks [18] (see Methods).

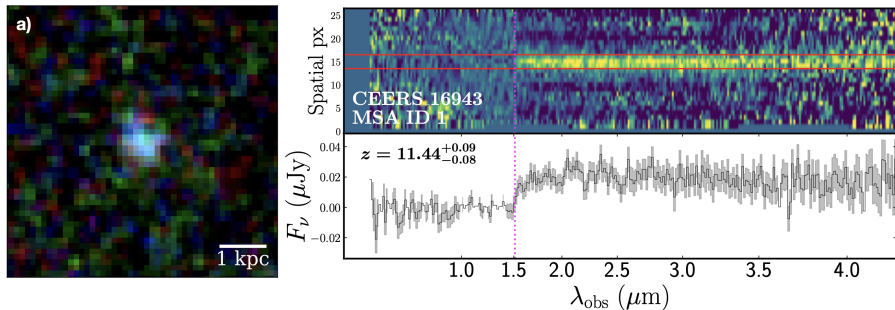


Fig. 2 a) A color image of Maisie’s Galaxy, showing approximately the true rest-ultraviolet color (made from the F277W, F356W, and F444W images). The blue color is indicative of low dust attenuation and a fairly young stellar population. b) The region of Maisie’s Galaxy’s spectrum around the detected Ly α break. The top panel shows the 2D spectrum as the bright trace, with the negative “shadows” representing the subtractions of the individual nods. The red horizontal lines show the spatial extent over which the 1D spectrum, shown in the bottom panel, was extracted. A clear spectral break is seen, below which there is no significant flux. We interpret this as the Ly α break at a redshift of 11.44, which represents a time 390 Myr after the Big Bang.

We used several methods to measure the wavelength of the spectral break (see Methods and Table 2). Interpreting this feature as the Ly α break (Fig. 2b) yields a redshift $z = 11.44^{+0.09}_{-0.08}$, consistent with photometric redshift estimates. Performing stellar population modeling (see Methods for details) on the observed photometry of this galaxy, fixing the redshift to this spectroscopic value, we confirm earlier results [7, 12] that Maisie’s Galaxy is a modestly massive ($\log_{10} M_*/M_\odot = 8.4^{+0.3}_{-0.4}$), dust-poor ($A_V = 0.07^{+0.09}_{-0.05}$ mag) galaxy, with a high star-formation rate for its stellar mass ($\log_{10}(\text{SFR}/M_*) = -8.0^{+0.4}_{-0.5} \text{ yr}^{-1}$).

NIRSpec observations of star-forming galaxies at $z < 9.6$ frequently detect strong [O III] and H β emission lines [24–27] that shift beyond the instrument’s spectral coverage for redshifts $z > 9.6$. Emission lines at blue optical and ultraviolet rest-frame wavelengths are typically weaker and harder to detect in low signal-to-noise ratio (S/N) spectra. The observed spectrum of Maisie’s Galaxy shows no strong emission lines (a strong feature potentially consistent with emission from singly-ionized oxygen, [O II] rest-frame wavelength $\lambda_{\text{rest}} = 3727\text{\AA}$, observed at $4.6\mu\text{m}$, was discarded as a likely instrumental artifact – see the Methods section for further explanation). Exploring the rest-frame ultraviolet portion of the spectrum shows several weakly positive features. Specifically, there are positive emission features from doubly-ionized oxygen ([O III], rest-frame wavelength $\lambda_{\text{rest}} = 1666\text{\AA}$) and doubly-ionized carbon (C III], $\lambda_{\text{rest}} = 1909\text{\AA}$) at a redshift of $z = 11.383$. However, we estimate that these emission lines are significant at only the 2–3 σ level. Thus we do not consider them robust detections, though they would corroborate the Ly α -break derived redshift.

The spectrum of CEERS-93316 (Figure 3) shows emission lines from the hydrogen Balmer series, [O III], [O II], and [S II] ($\lambda_{\text{rest}} = 6718, 6733\text{\AA}$) at a redshift $z = 4.912 \pm 0.001$. This is the same redshift as the galaxy CEERS-DSFG-1

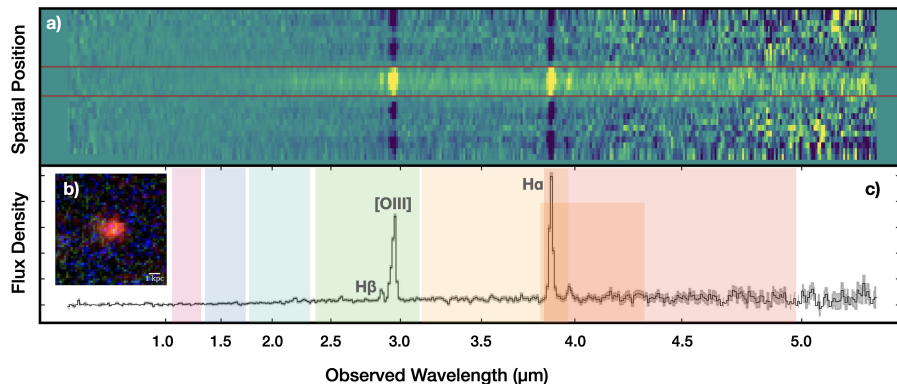


Fig. 3 The NIRSpect spectrum of CEERS-93316. Similar to Figure 2, Panel a shows the 2D spectrum with the red lines denoting the spatial extraction limits, and Panel c shows the 1D extraction. Clear emission lines can be seen in both panels, which we label in the bottom panel. The bottom panel also illustrates the wavelengths covered by the *JWST*/NIRCam filter set used to select this galaxy, highlighting how [O III] contamination in F277W (green) and H α contamination in *all* of F356W (yellow), F410M (orange) and F444W (red) conspired to mimic the signature of both a very high-redshift Ly α break and a blue continuum at longer wavelengths. This unusual (but educational) situation is detailed further in Figure 4. Panel b shows a F150W+F200W+F277W color image of this galaxy.

(MSA ID 2), which lies 26 arcsec away and was previously discussed by [22] as a moderate-redshift galaxy with colors that could mimic a high-redshift Ly α break. This redshift is also consistent with the alternative lower-redshift solution proposed for CEERS-93316 [8, 20–22], and the same redshift as (at least) two other neighboring galaxies (see Methods). The continuum emission of CEERS-93316 fades at wavelengths shorter than $2.5 \mu\text{m}$ (rest frame $\lesssim 0.4 \mu\text{m}$), although flux is significantly detected in the spectrum down to $\lambda \approx 1.2 \mu\text{m}$. The strong H α ($\lambda_{\text{rest}} = 6564\text{\AA}$) and [O III] lines have large rest-frame equivalent widths ($790 \pm 140\text{\AA}$ and $1020 \pm 180\text{\AA}$ respectively), and hence contribute significantly to the flux measured by NIRCcam through the F277W, F356W, F410M, and F444W filters (specifically, at this precise redshift, H α emission actually contributes to the flux in the last three of those filters; Figure 3). The combination of the strong lines and the red continuum leads to the red colors measured between filters F150W, F200W, and F277W and the blue colors from F277W to F444W (Figure 1b).

The significant reddening implied by the relative lack of observed UV continuum flux is corroborated by the large Balmer decrement measured from the spectrum ($\text{H}\alpha/\text{H}\beta = 5.6 \pm 0.6$), which implies - despite the large equivalent widths of the lines - a substantial nebular color excess of $E(B - V)_{\text{nebular}} = 0.71 \pm 0.12$ assuming a Cardelli extinction law (see Methods). Indeed such scenarios have been considered as alternative explanations for the colors of CEERS-93316 [8, 20, 22]. An active galactic nucleus could also be responsible for strong line emission in an otherwise older galaxy [e.g., 28, 29].

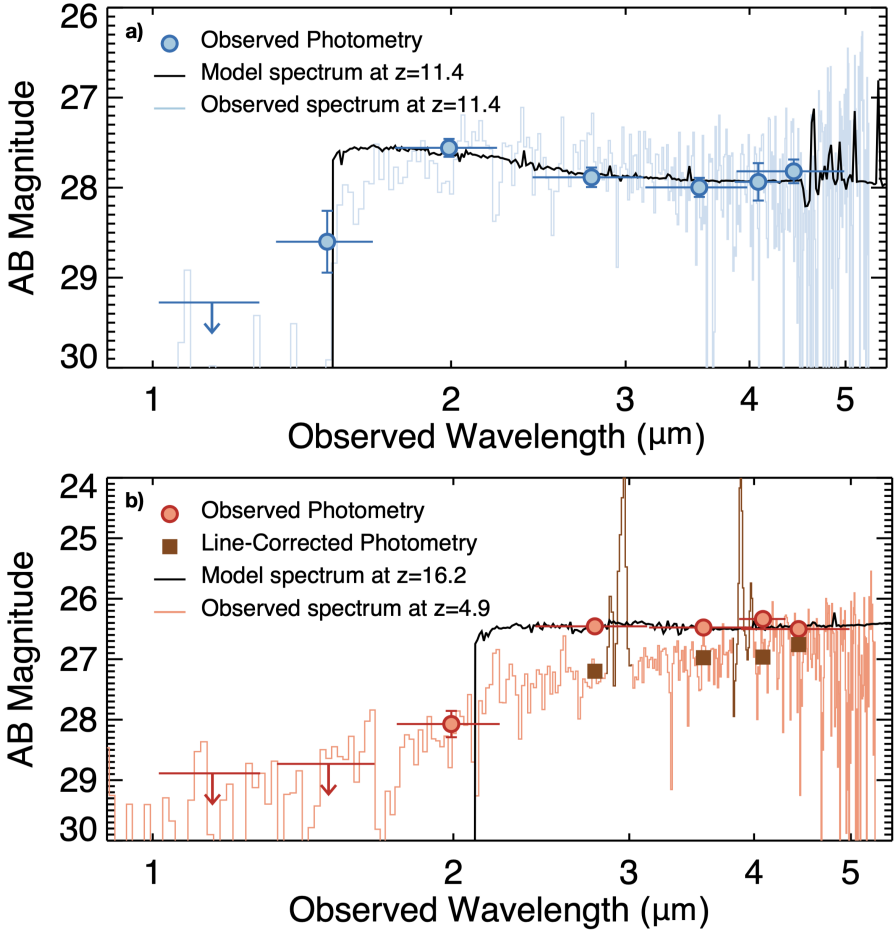


Fig. 4 Spectral energy distributions for Maisie's Galaxy (a), and for CEERS-93316 (b). Both panels show the observed photometry compared to the best-fitting stellar population model (black) and the observed spectra. In the bottom panel, the model is deliberately shown at $z = 16.2$ (consistent with the original photometric redshift) to demonstrate the way in which strong emission lines impact the observed photometry, conspiring in this specific (and somewhat unusual) case to replicate the presence of the Ly α break at $z \simeq 16$ and an apparently blue continuum at longer wavelengths. The squares show the observed photometry with the spectroscopic emission line contributions (shaded brown in the spectrum) removed.

The example of CEERS-93316 is a reminder that the prevalence of very strong nebular line emission in early galaxies can influence broad-band photometry with instruments such as *JWST*/NIRCam and mimic the colors predicted for much more distant objects [22]. Exceptional candidates for galaxies at extreme redshifts require spectroscopic confirmation. However, we note that this is a fairly extreme case, as it is only at very specific redshifts that

Table 1: Summary of Galaxy Properties

Property	Maisie’s Galaxy	CEERS-93316
RA (J2000)	214.943152	214.914550
Dec (J2000)	52.942442	52.943023
Photometric Redshift	$11.08^{+0.36}_{-0.39}$	$16.45^{+0.45}_{-0.18}$
Spectroscopic Redshift	$11.44^{+0.09}_{-0.08}$	4.912 ± 0.001
$\mathcal{T}_{\text{BigBang}}$ (Myr)	391	1195
$\log(M_{\star}/M_{\odot})$	$8.4^{+0.3}_{-0.4}$	$8.5^{+0.1}_{-0.1}$
A_V (mag)	$0.07^{+0.09}_{-0.05}$	$1.46^{+0.29}_{-0.43}$
$\log(\text{sSFR}/\text{yr}^{-1})$	$-8.0^{+0.4}_{-0.5}$	$-8.0^{+0.1}_{-0.1}$

Table 1 All uncertainties listed are 68% confidence intervals. The photometric redshift calculation is described in the Methods and has been updated for this work. We list here the spectroscopic redshift derived from the method with the smallest uncertainty for a given source; see Methods for a full discussion. $\mathcal{T}_{\text{BigBang}}$ denotes the age of the universe at the spectroscopic redshift. The stellar population properties are derived from Bagpipes.

strong emission lines can fully mimic a Ly α break with multiple broad-band filter detections.

Fortunately *JWST*/NIRSpec is a powerful tool for spectroscopic analysis and redshift measurement, as demonstrated by our observations of Maisie’s Galaxy and three other galaxies at $7.9 < z < 10.1$ (discussed in Methods). NIRSpec observations have now confirmed redshifts for 9 galaxies at $z \gtrsim 10$ [18, 30, Arrabal Haro in preparation], including two with $M_{\text{UV}} < -20$, unexpectedly bright compared to most pre-*JWST* predictions.

These confirmations are crucial to improving our physical understanding of the first phases of galaxy formation. Early analyses of *candidate* galaxies at $z = 10$ –12 have shown that their observed abundance is significantly higher than predicted by nearly all theoretical models [e.g., 7, 10, 12]. This could indicate that specific assumptions in these models need to be modified at very high redshifts, including an increased efficiency of converting gas into stars at the earliest times or even a higher characteristic star mass in these early epochs. Such a “top-heavy” initial mass function has indeed been predicted to be present in early galaxies, driven by a combination of their chemically simple makeup [e.g., 31, 32] as well as a rising cosmic microwave background temperature floor [e.g., 33]. However, before any such unusual physical properties can be robustly inferred for early galaxies, their photometric redshift estimates must be verified. The NIRSpec confirmation of Maisie’s Galaxy at $z = 11.4$ reported here, combined with growing numbers of $z \gtrsim 10$ spectroscopic confirmations in the literature [e.g., 18], show that well-established methods of photometrically selecting galaxies work robustly at $z \sim 10$ –12.

Methods

Near-Infrared Imaging data and Source Selection

We select high redshift galaxy candidates from the first epoch of imaging from the Cosmic Evolution Early Release Science (CEERS; PI: S. Finkelstein [7]) survey. These data consist of four roughly contiguous pointings with the

NIRCam instrument on *JWST*, covering an area of ~ 35 arcmin². The full area is covered by six broad-band filters (F115W, F150W, F200W, F277W, F356W, F444W) and one medium-band filter (F410M). We use the v0.5 data release from the CEERS team¹ [17]. These reductions use the STScI *JWST* pipeline with several custom modifications, correcting for various issues, including $1/f$ noise, wisps, and snowballs, with updated photometric calibration from late 2022. The 5σ photometric depths of these data for compact source detection are ~ 29 – 29.2 AB magnitudes in F115W, F150W, F200W, F277W and F356W, and ~ 0.7 and ~ 0.5 mag shallower in F410M and F444W, respectively.

Spectroscopic observations targeted three primary galaxy candidates: CEERS J141946.36+525632.8, aka “Maisie’s Galaxy” [7], with photometric redshift $z \approx 11.1$, “CEERS-93316” with photometric redshift $z \approx 16.4$ [8], and CEERS-DSFG-1, a *JWST*-detected galaxy with millimeter-wavelength emission that is likely to arise from dust-obscured star formation at $z \sim 5$, but whose near-infrared colors could be interpreted as suggesting $z > 10$ [22]. These object names come from the original papers reporting these objects rather than from a homogeneous source catalog. Essential parameters of the first two galaxies, including results from the present analysis, are summarized in Table 1. Detailed analysis of CEERS-DSFG-1 will be presented elsewhere.

Photometry was optimized for accurate measures of colors, generally following [12], with a few key updates to improve measured colors, particularly between *HST* and *JWST*. Specifically, all bands with PSFs smaller than that of F277W (i.e., ACS F606W, F814W, and NIRCam F115W, F150W, and F200W) were convolved to match the F277W PSF. For the remaining images, fluxes were measured in the native images, but a correction was applied on a per-source basis as the ratio of the flux in the native F277W image to that of the F277W image convolved to match the PSF in a given larger-PSF image. We then used simulation-based corrections to derive accurate total fluxes. Photometric redshifts were derived using EAZY [34], including new custom templates designed to match the expected blue colors of early galaxies [35].

NOEMA Data and Analysis

Observations with the JCMT and SCUBA2 bolometer array detected tentative $850\ \mu\text{m}$ emission in the vicinity of CEERS-93316. [22] showed that such a detection is unlikely to come from a $z > 10$ object and explored different scenarios to explain the colors of this high-redshift galaxy candidate, finding that a $z \sim 4.8$ galaxy with some dust attenuation and strong emission lines could also explain the measured photometry.

We observed dust continuum with band 3 of the Institut Radio Astronomie Millimétrique (IRAM) NOrthern Extended Millimeter Array (NOEMA) as a Director’s Discretionary Time (DDT) program #D22AC001 (PI: S. Fujimoto). The observations were carried out between 2022 Nov 26 and 2022 Dec 08 in several visits with the C configuration using 10–11 antennas. The data were

¹<https://ceers.github.io>

processed in the standard manner with the pipeline using the latest version of the GILDAS software. We used CASA version 6.5 for the imaging [36].

The upper and lower side bands of the band 3 receiver were tuned to 256.6 GHz and 271.1 GHz, resulting in the central wavelength of 1.134 mm. The observations of 3c345, 3c273, J1439+499, and 3c84 served as band-pass phase calibrators. Additional targets 1418+546 and J1439+499 were used for the phase and amplitude calibrations. We calibrated the absolute flux scale against MWC349, LkHa101, and 2010+723 whose flux densities are regularly monitored at NOEMA. The total integration time on-source was 6.5 hours.

To maximize sensitivity, we used natural weighting for the imaging. The resulting 1 mm continuum map has synthesized beam FWHM of $0.''91 \times 0.''67$ with 1σ sensitivities of $28 \mu\text{Jy beam}^{-1}$ for the continuum. We do not identify any line features at the target position and thus produce the 1 mm continuum map from all channels.

In Figure 5, we show the NOEMA 1.1-mm intensity contours overlaid on the NIRC*am* color image around CEERS-93316. We do not detect emission at the position of CEERS-93316, with a 3σ upper limit of $0.084 \text{ mJy beam}^{-1}$. This provides an upper limit of its dust-obscured star formation rate of $\sim 20\text{--}200 M_{\odot} \text{ yr}^{-1}$ with a modified black body with dust temperature $T_{\text{d}} = 40\text{--}70 \text{ K}$ and a typical spectral index of $\beta_{\text{d}} = 1.8$, being consistent with the SFR estimate of $20 \pm 10 M_{\odot}/\text{yr}$ reported by [22]. This rules out the possibility that CEERS-93316 is a dusty starburst galaxy with $\text{SFR} \gg 200 M_{\odot} \text{ yr}^{-1}$, while a moderately star-forming ($\text{SFR} < 200 M_{\odot} \text{ yr}^{-1}$) dusty star-forming galaxy scenario remains.

On the other hand, the NOEMA observations revealed relatively bright continuum emission from a nearby ($\sim 1.''5$) galaxy at 9σ significance. We estimate $0.56 \pm 0.07 \text{ mJy}$ with an optimized aperture. This is in good agreement with the previous report of SCUBA2 $850 \mu\text{m}$ emission of $0.64 \pm 0.26 \text{ mJy}$ [22], implying that this neighboring galaxy is the main contributor to the aforementioned detection.

Near-Infrared spectroscopy and data reduction

JWST/NIRSpec multi-object spectroscopic observations (DDT program #2750; PI: P. Arrabal Haro) were executed on UTC 2023 March 24-25 using the PRISM/CLEAR combination of disperser and filter. The Micro Shutter Array [MSA; 37] was configured to observe 147 faint-object targets. The observations consisted of 3 sequences of 3 nodded integrations, each with 9 to 10 readout groups in NRSIRS2 readout mode, for a total combined exposure time of 18387 s.

Three-shutter slitlets were employed, enabling a three-point nodding pattern to facilitate background subtraction. The prism disperser covers the wavelength range 0.6 to $5.3 \mu\text{m}$ with varying spectral resolution $R \equiv \lambda/\Delta\lambda \approx 30$ at $\lambda = 1.2 \mu\text{m}$ to > 300 at $\lambda > 5 \mu\text{m}$. The low resolution of the prism at bluer wavelengths aids the detection of faint UV continuum and the Ly α

break, while the higher resolution at red wavelengths facilitates the detection of redshifted optical rest-frame emission lines.

The MSA configurations included a total of 6 NIRC*am*-selected $z \gtrsim 8.5$ galaxy candidates as well as 141 other targets. We report results on 9 high-redshift candidates in Table 2 including the primary targets described above.

The NIRS*pec* data processing followed the methodology employed for other CEERS NIRS*pec* prism observations [25]. We make use of the STS*ci* Calibration Pipeline² version 1.8.5 and the Calibration Reference Data System (CRDS) mapping 1069. We use the `calwebb_detector1` pipeline module to subtract the bias and the dark current, correct the $1/f$ noise, and generate count-rate maps (CRMs) from the uncalibrated images. The parameters of the `jump` step are modified for an improved correction of “snowball” events³ associated with high-energy cosmic rays.

The resulting CRMs are then processed with the `calwebb_spec2` pipeline module which creates two-dimensional (2D) cutouts of the slitlets, performs the background subtraction making use of the 3-nod pattern, corrects the flat-fields, implements the wavelength and photometric calibrations and resamples the 2D spectra to correct the distortion of the spectral trace. The `pathloss` step accounts for the slit loss correction at this stage of the reduction process. Instead, when required for the analysis, we introduce slit loss corrections based on the morphology of the sources in the NIRC*am* bands and the location of the slitlet hosting them.

The images of the three nodds are combined at the `calwebb_spec3` pipeline stage, making use of customized apertures for the extraction of the one-dimensional (1D) spectrum. The custom extraction apertures are visually defined for targets presenting high S/N at the continuum or emission lines when they are easily recognizable in the 2D spectra. For those cases where the targets are too faint for a robust visual identification, a 4-pixel extraction aperture is defined around a spatial location estimated from the relative position of the target within its shutter, derived from the MSA configuration.

The 2D and 1D spectra are simultaneously inspected with the Mosviz visualization tool⁴ [38] to mask possible remaining hot pixels and other artifacts in the images, as well as the detector gap (when present). Data from the three consecutive exposure sequences are combined after masking image artifacts to produce the final 2D and 1D spectral products.

The *JWST* pipeline uses an instrumental noise model to calculate flux errors for the extracted spectra. We test and rescale these flux errors for the effect of data correlation introduced by the pipeline following procedures described elsewhere [39].

²<https://jwst-pipeline.readthedocs.io/en/latest/index.html>

³<https://jwst-docs.stsci.edu/data-artifacts-and-features/snowballs-and-shower-artifacts>

⁴<https://jdaviz.readthedocs.io/en/latest/mosviz/index.html>

Redshift estimation

In this paper, we focus on “high-priority” galaxies observed, which were selected based on either highly-likely high-redshift solutions, with one additional source which showed a possible high-redshift solution but was more likely to be at lower redshift (MSA ID 2, discussed in [22]). For objects with multiple clear emission lines, we were easily able to identify the [O III] and/or H α emission lines. Spectroscopic redshifts are measured by comparing the observed emission lines with their theoretical vacuum transitions. A Gaussian profile is fitted for every spectral line to establish the transition wavelength. The Gaussian fluxes are used to weigh the mean redshifts in Table 2. In those observations, where the [O III] 4960,5008 Å doublet lines are merged, the profile fitting assumes the same gas kinematics and their amplitudes fixed by the theoretical emissivity ratio (2.98 see [40]) to isolate them.

We also estimated the redshifts using the detected continuum with two methods. The first one consists in fitting the wavelength of the Ly α break when it was observed. We do this following the method detailed in [39]. In summary, we create a five-parameter model to describe an object’s spectrum. We first create the intrinsic spectrum based on the redshift, UV absolute magnitude, and UV spectral slope. We then add IGM absorption by zeroing out the spectrum below 1215.67 Å rest-frame wavelength, and add Ly α damping wing absorption by adding two additional parameters: the neutral hydrogen fraction (x_{HI}) and an ionized bubble radius (R_{bubble}), following [41] and [18]. We derive posterior constraints on these five parameters using an IDL implementation of the EMCEE Python code (see [42] for details), restricting the spectrum to wavelengths below 2500 Å rest-frame for a given redshift. We performed a similar analysis using the MCMC sampler package from [43], finding broadly similar results, with most redshifts consistent to within $\Delta z \sim 0.1$. The second method is full spectral fitting to the NIRSPEC data, which detects the continuum for all our galaxies, using the EZY [34] and a variety of spectral templates, including UV-bright and dusty galaxies. We remark that for Maisie’s Galaxy, the spectrum covers both the Lyman and Balmer breaks. All methods provide results consistent within $\Delta z \sim 0.1$, consistent within our estimated uncertainties.

Redshift results

We derive emission-line redshifts for galaxies with MSA IDs 0 (CEERS-93316, [8]; via [O II], [O III], H α), 2 ([22]; via [O III], H α), 28 (via [O II], [O III] and 355 (via [O III]), and Ly α break redshifts for MSA IDs 1 (Maisie’s Galaxy; [12]), 28, 64 and 355. Source ID 69 shows a weak break at $\sim 1.3\mu\text{m}$, and this methodology does find a maximum likelihood of $z = 9.744$. However, the result has a large uncertainty, with a significant probability of the redshift being lower. We thus do not consider ID=69 confirmed. We present our redshift measurements in Table 2.

For Maisie’s Galaxy, we considered the alternative interpretation of a Balmer break at $z = 3.114$. Assuming that redshift and integrating the

observed spectrum in f_λ units through wavelength intervals 3145-3563 Å and 3751-4198 Å [18] we measure signal-to-noise ratios of 0.0 and 9.9 below and above the break, and a 3σ limit on the flux ratio > 2.6 , which is considerably larger than would be predicted from stellar population synthesis models [18]. This supports the higher redshift interpretation of the break resulting from Ly α opacity of the IGM.

We note that the derived spectroscopic redshifts are in broad agreement with the photometric redshift. For Maisie’s Galaxy, in particular, the photometric redshift has been modified since the galaxy was discovered as data processing improved. The galaxy was originally thought to be at $z \sim 14$, but the photometric redshift was revised to $z = 11.8_{-0.3}^{+0.2}$ after improved astrometric registration recovered weak flux in F150W [7]. Improved NIRCcam zero-point flux calibration revised this further to $z = 11.5_{-0.6}^{+0.2}$ [12], while the latest photometric redshift from the photometry described in this paper (which is updated over that described in [12] to better match *HST* and *JWST* photometry) suggests $z = 11.08_{-0.39}^{+0.36}$, consistent within the errors with our break-based redshift of $z = 11.44_{-0.08}^{+0.09}$.

CEERS-93316 and the millimeter-detected galaxy CEERS-DSFG-1 (MSA ID 2) both have redshifts $z = 4.91$. We identify two more galaxies (MSA IDs 2763 and 3149) at nearly the same redshift in the NIRSpc observations (Fig. 7, Table 2), supporting the hypothesis of a physical overdensity [20]. Moreover, the NOEMA-detected galaxy 1.5 arcsec from CEERS-93316 (Fig. 5) has a very similar photometric redshift and may well also be associated, but still requires spectroscopy.

Emission lines

The combined spectrum of “Maisie’s Galaxy” exhibits a particularly strong emission feature at $\sim 4.6 \mu\text{m}$ resembling a bright emission line. According to the redshift estimated from the Ly α break, the only possible explanation for this line to be real is [O II]. However, detailed analysis of individual nods revealed the presence of image defects that could be affecting this wavelength region. Hence, we do not consider this to be a real emission feature of the galaxy. Moreover, such a strong emission line being physical would necessarily imply four clear negative patterns above and below it in the 2D spectrum, a product of the noded background subtraction and posterior combination (see the 2D spectra of MSA ID 28 and 355 in Figure 6). This is not the case for this hypothetical line, which suggests that it is indeed an artifact. All calculations performed with this spectrum were done after masking the spurious emission to avoid possible biases in the results it may cause.

We also note that the observed strength of this putative [O II] emission is not expected. This galaxy’s blue spectral slope implies a young, fairly low-metallicity stellar population (consistent with the low SED-fitting-derived dust attenuation). Such a stellar population should exhibit a fairly weak [O II] line, with a high [Ne III]/[O II] ratio [e.g., 26]. While the [Ne III]3869 line would be observed redder than [O II] where the noise is somewhat higher, should

the initially observed [O II] flux be real, we would expect a significant detection. However, the maximum signal-to-noise (SNR) within a few pixels of the expected position is ~ 1 after continuum subtraction.

To explore what other constraints could be placed on emission lines in Maisie's Galaxy, we took the spectrum and subtracted the continuum emission as a rolling 40-pixel average. We then explored whether any pixels had a SNR of greater than two, finding no such pixels. We do find pixels with SNR just below 2 coincident with the expected observed wavelengths for O III]1660 and C III]1909 at $z = 11.383$, which would be the spectroscopic redshift if the [O II] emission were real. Given the low significance of these emission features, we do not consider these lines to be detected. However, if future deeper spectroscopy finds these to be robust, it would be consistent with our derived break redshift within the uncertainties.

The emission lines in CEERS-93316 were fitted manually from the spectrum by first subtracting a local continuum and fitting Gaussian profiles to the visible emission lines. In the case of the blended but partially-resolved [O III] 4960,5007 lines, a double Gaussian function was fitted. The Balmer lines ($H\alpha$ and $H\beta$) were corrected for underlying stellar absorption using the best-fitting stellar continuum from the Bagpipes fits (a $< 2\%$ correction in both cases; see below for a description of the Bagpipes fits). As described in the main text, these lines have large rest-frame equivalent widths ($790 \pm 140\text{\AA}$ and $1020 \pm 180\text{\AA}$ for [O III] and $H\alpha$, respectively), and thus significantly affect the long-wavelength NIRC*am* fluxes, mimicking the signature of a $Ly\alpha$ break.

Spectral energy distribution fitting

We use three spectral energy distribution (SED) fitting codes to derive physical properties for our galaxies, Bagpipes [44], Cigale [45], and Synthesizer [46]. We apply several different methods to more thoroughly explore plausible values for the physical properties of these galaxies, as results obtained from SED fitting are known to be highly sensitive to the priors applied [47, 48], with different codes often returning a range of different values [49]. The photometric fluxes we fit are taken from [12], and we incorporate redshift constraints based on our new spectroscopic data. We describe in detail the approaches taken by each of these three codes separately below.

Bagpipes

Our Bagpipes fits make use of the 2016 updated version of the [50] stellar population models. Nebular emission lines and continuum are included in the model using results from the Cloudy photoionization code [51]. Dust attenuation is included using a flexible-slope model, which also includes a Drude profile to model the 2175\AA dust bump and an additional factor multiplying the attenuation applied to star-forming regions (which we take to include all stellar emission arising from stars younger than 10 Myr and all resulting nebular emission) [52]. The details of our Bagpipes model assumptions are identical to

those used in [8, 53]. In particular, we use a constant star-formation history model, shown to produce stellar ages and stellar masses at the lower end of the plausible range for objects of interest. We apply a Gaussian prior to the redshift of each object based on our new spectroscopic data, with a standard deviation of 0.15 in each case. The median value for our Gaussian prior is set to $z = 11.4$ for Maisie’s Galaxy and $z = 4.9$ for CEERS-93316.

Cigale

For this work, we use the last version of Cigale [54, 55], with updated emission line models computed from Cloudy [51]. For the dust, a Calzetti [56] extinction law is adopted for the dust attenuation of the stellar continuum. However, the nebular emission (continuum and lines) is attenuated with a screen model and a Small Magellanic Cloud (SMC) extinction curve [57]. No 2175Å dust bump is added. We select a so-called “*delayed + burst*” SFH with $\text{SFR} \propto t \times \exp(-t/\tau)$. Both the stellar and the gas metallicities are allowed to vary from low values $Z = 0.0004$ to Z_{\odot} in the fit. As for Bagpipes, the mean value for our Gaussian prior is set to $z = 11.4$ for Maisie’s Galaxy, and $z = 4.9$ for CEERS-93316. For CEERS-93316, we use constraints from the equivalent widths measured on the NIRSpc spectrum of $\text{H}\alpha$, $\text{H}\beta$, and the two $[\text{O III}]$ lines. The derived equivalent widths estimated are in excellent agreement with $0.7 \leq \text{EW}_{\text{measured}}/\text{EW}_{\text{CIGALE}} \leq 1.3$.

Synthesizer

For the Synthesizer run, we explored star formation histories described by a delayed exponential with timescales ranging from 1 Myr to 100 Myr (i.e., from instantaneous to nearly constant star formation histories). We considered stellar populations models from [58], a [59] initial mass function, and metallicities smaller than the solar value. The nebular continuum and lines are included in the modeling as described in [46], with an attenuation law and differential nebular-stellar dust effects as described in [60]. Redshifts are fixed to the values given in Table 2. For CEERS-93316, $\text{H}\alpha$ and $\text{H}\beta$ equivalent widths were included in the fits, but all models provided lower values than those measured by a factor of ~ 4 . For Maisie’s Galaxy, a relatively strong degeneracy in the age was observed depending on the strength of the Balmer break, which is constrained by the spectroscopic data with limited SNR. Fitting data points bluewards of the Balmer break implied younger mass-weighted ages and smaller stellar masses (30 ± 10 Myr, $\log_{10} M_*/M_{\odot} = 8.3 \pm 0.1$). Including NIRSpc spectroscopic data points redwards of the Balmer break increased ages and masses (120 ± 30 Myr, $\log_{10} M_*/M_{\odot} = 8.8 \pm 0.1$).

Data Availability. The JWST NIRSpc data are available from the Mikulski Archive for Space Telescopes (MAST; <http://archive.stsci.edu>), under program ID 2750. The CEERS JWST imaging data are available from MAST under program ID 1345. Reduced NIRCcam data products from the CEERS team are available at <https://ceers.github.io>.

Code Availability. JWST NIRSpec data were reduced using the JWST Pipeline (Version 1.8.5, reference mapping 1069; <https://github.com/spacetelescope/jwst> NIRSpec data inspection used the Mosviz visualization tool (<https://jdaviz.readthedocs.io/en/latest/mosviz/index.html> [38]). Photometric redshifts were measured using EAZY [34]. The Synthesizer code to perform stellar population synthesis modeling of galaxy spectro-photometric data is described in [46, 61]. The emission line profiles were fitted and their fluxes measured using LIME [62] (<https://lime-stable.readthedocs.io>). The Bagpipes code used for stellar population synthesis modeling is described in [44] and is available at (<https://bagpipes.readthedocs.io>). A detailed description of the Cigale code can be found in [54, 55]. Cigale allows to fit data from the X-ray to the radio range and offers the possibility to add a contribution from an active galactic nucleus (AGN) and also to have constraints from non-photometric data (line fluxes, equivalent width, luminosities, or any physical parameter given in the input table). For this paper, we use a non-public version that fits photometric and spectroscopic data together. Cigale is available from (<https://cigale.lam.fr/>).

Acknowledgments. PAH, MED, SLF, and JSK acknowledge support from NASA through STScI ERS award JWST-ERS-1345. SLF acknowledges support from the University of Texas at Austin. PGP-G acknowledges support from Spanish Ministerio de Ciencia e Innovación MCIN/AEI/10.13039/501100011033 through grant PGC2018-093499-B-I00. ACC acknowledges support from the Leverhulme Trust via a Leverhulme Early Career Fellowship. CTD, DJM, RJM, and JSD acknowledge the support of the Science and Technology Facilities Council. FC acknowledges support from a UKRI Frontier Research Guarantee Grant [grant reference EP/X021025/1]. MHC acknowledges financial support from the State Research Agency (AEIMCINN) of the Spanish Ministry of Science and Innovation under the grants “Galaxy Evolution with Artificial Intelligence” with reference PGC2018-100852-A-I00 and “BASALT” with reference PID2021-126838NB-I00. VF acknowledges support from ANID through FONDECYT Postdoc 2020 project 3200340. RA acknowledges support from ANID through FONDECYT Regular 1202007.

This work is based on observations with the NASA/ESA/CSA James Webb Space Telescope obtained from the Mikulski Archive for Space Telescopes at the STScI, which is operated by the Association of Universities for Research in Astronomy (AURA), Incorporated, under NASA contract NAS5-03127.

This work is partially based on observations carried out under project number D22AC with the IRAM NOEMA Interferometer. IRAM is supported by INSU/CNRS (France), MPG (Germany), and IGN (Spain).

Author Contributions. PAH led the JWST NIRSpec DDT observing proposal, the observation design, the data reduction, and contributed extensively to text and figures. MD, SLF, and JSK contributed extensively to spectroscopic target selection and prioritization, with extensive input from many authors including CTD, ACC, FC, JSD, SF, CP, PGP-G, DDK, DJM, RJM, and JAZ.

Galaxy redshifts were measured primarily by PAH, VF, SLF, PPP-G, SF, IJ, and RLL. RLL and VF measured emission line properties; FC and JRT analyzed implications from the emission lines. DB, ACC, and PGP-G modeled and interpreted the spectral energy distributions of the galaxies. SF led the NOEMA observing program with contributions to planning from several coauthors including JAZ and CMC, and MK contributed to NOEMA execution and data analysis. MD and SLF led the drafting of the paper text with contributions to text, figures, editing and formatting by PAH, SF, CP, PGP-G, HCF, MG, JAZ, TAH, KC, and other authors. MBB led data reduction for the CEERS NIRC*am* observations with extensive contributions by AMK and HCF. SHC and NP contributed to the NIRS*pec* proposal, and ROA, VB, MHC, DDK, RAL, and BJW (as well as many authors above) contributed to the discussion, analysis and interpretation.

Competing Interests. The authors declare that they have no competing financial interests.

Additional Information. Correspondence and requests for materials should be addressed to PAH (email: parrabalh@gmail.com).

Extended Data

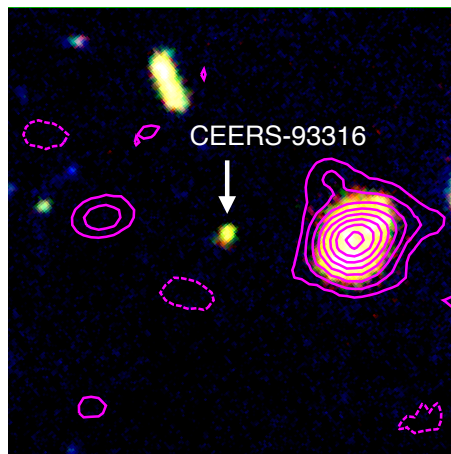


Fig. 5 NOEMA 1.1-mm contours overlaid on the NIRC*cam* $6'' \times 6''$ RGB color image (R: F444W, G: F356W, B: F200W) around CEERS-93316 marked with the white arrow. North is up and East is left. The magenta contours are drawn at 1σ interval from $\pm 2\sigma$ to $\pm 9\sigma$. We obtain the 3σ upper limit of 0.084 mJy from CEERS-93316, while the continuum is robustly detected from a nearby source, which attributes to the tentative SCUBA2 flux (0.64 ± 0.26 mJy [22]).

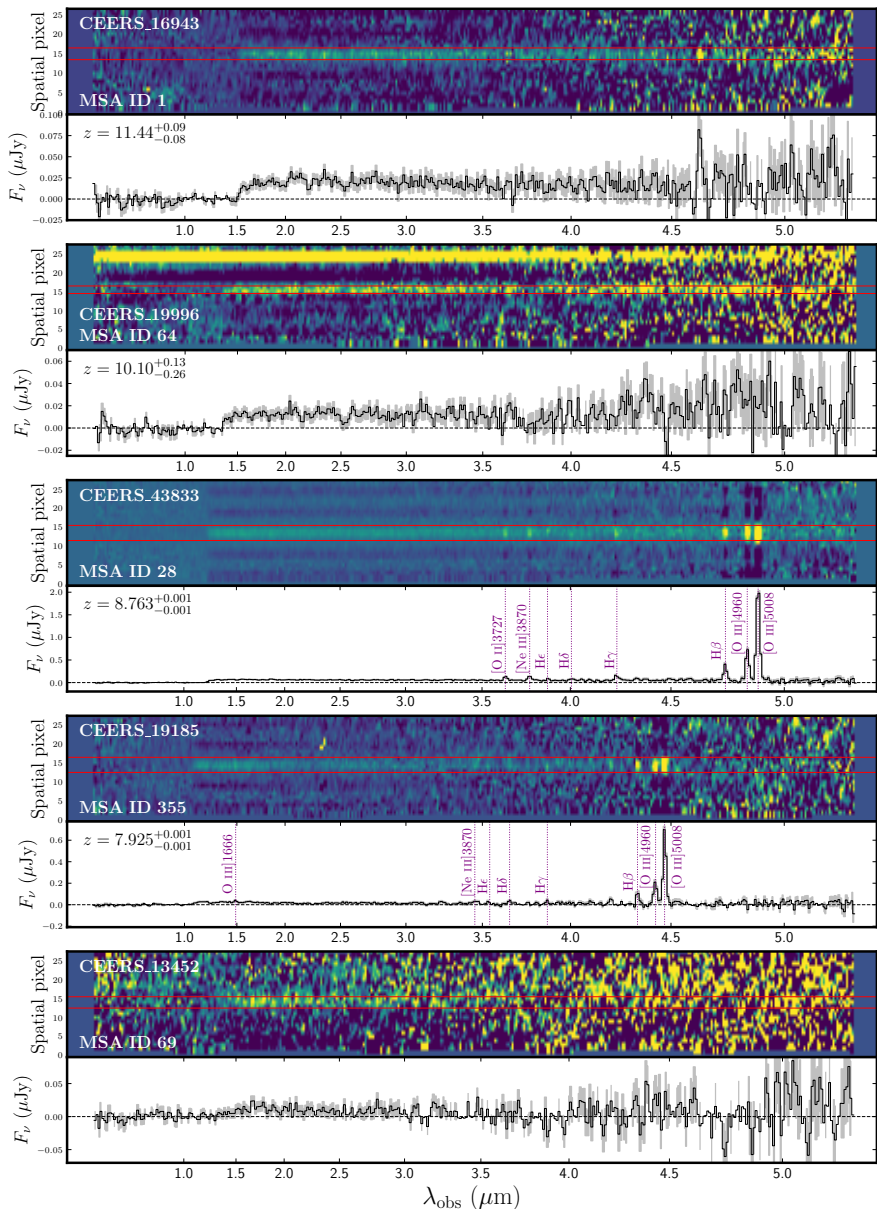


Fig. 6 2D and 1D NIRSpectra of five galaxies selected to have photometric redshifts $z > 8$, with spectral features and spectroscopic redshifts indicated, except for CEERS 13452 where we are unable to determine a redshift with confidence.

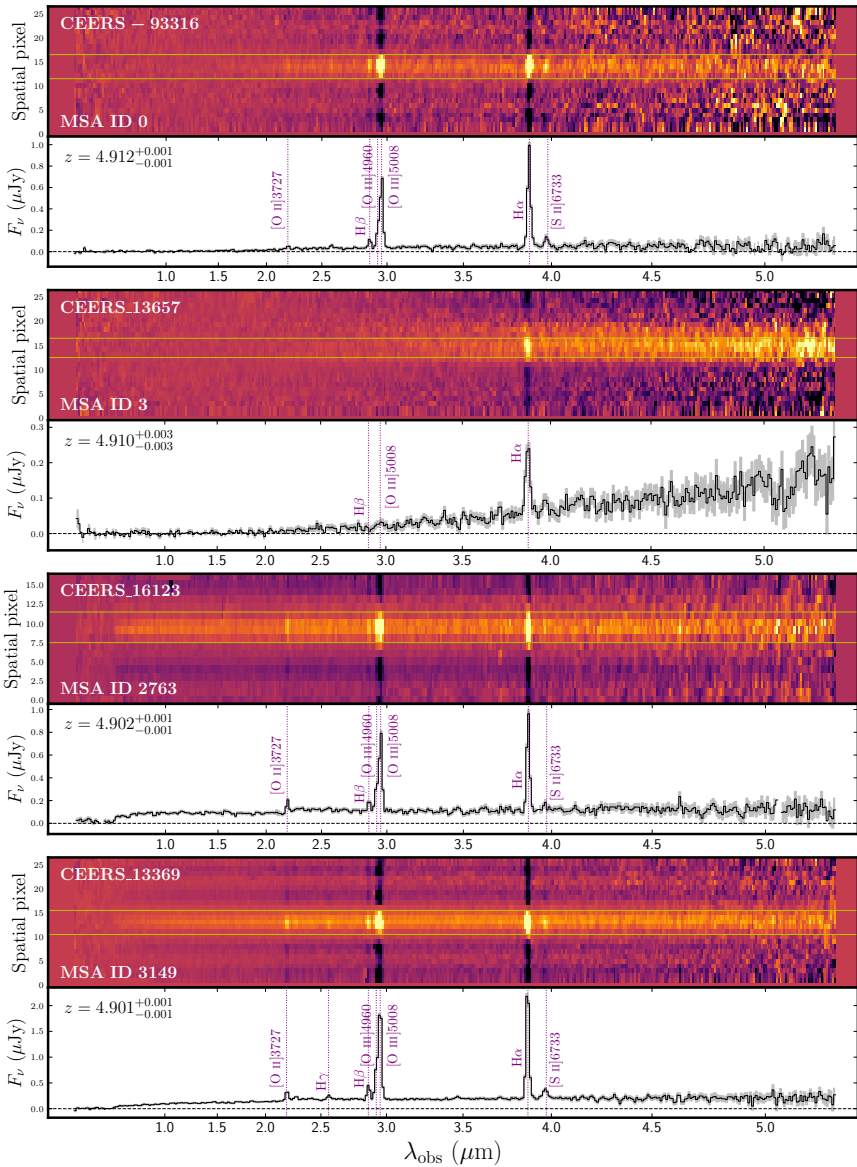


Fig. 7 2D and 1D NIRSpectra of CEERS-93316 and three other galaxies at similar redshifts $z \approx 4.9$, highlighting a potential overdensity in the field at this redshift.

Table 2: Summary of Spectroscopically Confirmed Galaxies

MSA ID	R.A. (J2000)	Dec (J2000)	F277W (AB)	z_{phot} 68% C.L.	$z_{\text{spec}}^{\text{lines}}$	$z_{\text{spec}}^{\text{break}}$	$z_{\text{spec}}^{\text{cont}}$
0	214.914550	52.943023	26.5	16.0–16.6	4.912 ± 0.001	—	$4.89_{-0.01}^{+0.01}$
1	214.943152	52.942442	27.9	10.7–11.5	—	$11.44_{-0.08}^{+0.09}$	$11.38_{-0.08}^{+0.14}$
2	214.909116	52.937205	26.2	3.4–13.6	4.910 ± 0.003	—	$4.88_{-0.01}^{+0.01}$
28	214.938642	52.911749	26.9	8.90–9.00	8.763 ± 0.001	$8.90_{-0.02}^{+0.04}$	$8.72_{-0.01}^{+0.01}$
64	214.922787	52.911529	28.3	10.4–11.6	—	$10.10_{-0.26}^{+0.13}$	$9.73_{-0.13}^{+0.21}$
69	214.861602	52.904604	28.2	9.5–10.3	—	—	—
355	214.944766	52.931450	28.7	8.0–8.5	7.925 ± 0.001	$7.71_{-0.10}^{+0.12}$	$7.88_{-0.01}^{+0.01}$
2763	214.927789	52.935859	25.1	4.87–5.44	4.902 ± 0.001	—	$4.87_{-0.01}^{+0.01}$
3149	214.914917	52.943622	24.7	0.88–4.81	4.901 ± 0.001	—	$4.87_{-0.01}^{+0.01}$

Table 3: Summary of Confirmed Galaxy Physical Properties

Software	MSA ID	Stellar Mass $\log_{10}(M_{\star}/M_{\odot})$	SFR $(M_{\odot} \text{ yr}^{-1})$	Stellar A_V (mag)
Bagpipes [44]	0	8.5 ± 0.1	4 ± 1	1.4 ± 0.4
	1	$8.4_{-0.4}^{+0.3}$	3 ± 2	$0.07_{-0.05}^{+0.09}$
Cigale [54, 55]	0	9.5 ± 0.2	8 ± 2	1.8 ± 0.3
	1	8.3 ± 0.5	8 ± 6	0.2 ± 0.1
Synthesizer [46]	0	8.8 ± 0.1	60 ± 20	2.3 ± 0.2
	1	8.6 ± 0.3	2 ± 1	0.1 ± 0.1

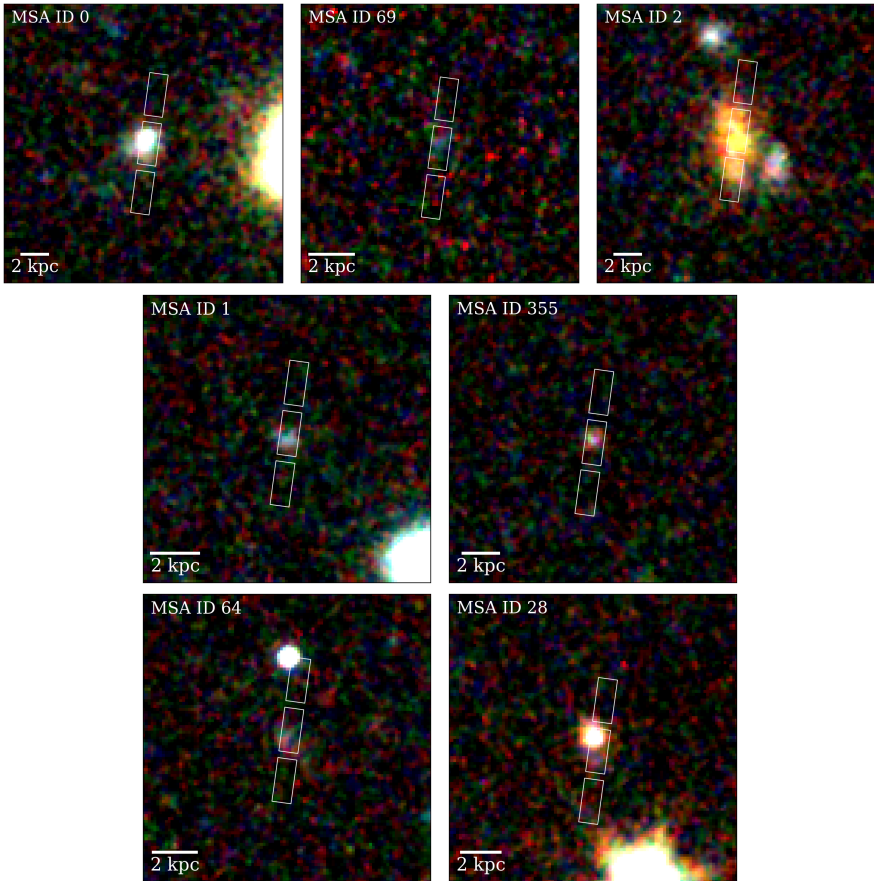


Fig. 8 Montage of images of the galaxies with spectroscopic confirmation presented here. Each image shows a $3'' \times 3''$ image centered on the location of each galaxy, with ID labeled. The red-green-blue image for each galaxy corresponds to the *JWST*/NIRCam F444W, F356W, and F277W, respectively, rotated with North up and East to the left. The rectangles show the approximate location of the *JWST*/NIRSpec MSA slit positions.

References

- [1] Bromm, V., Coppi, P. S. & Larson, R. B. The Formation of the First Stars. I. The Primordial Star-forming Cloud. *Astrophys. J.* **564**, 23–51 (2002).
- [2] Schneider, R., Ferrara, A., Natarajan, P. & Omukai, K. First Stars, Very Massive Black Holes, and Metals. *Astrophys. J.* **571**, 30–39 (2002).
- [3] Wise, J. H., Turk, M. J., Norman, M. L. & Abel, T. The Birth of a Galaxy: Primordial Metal Enrichment and Stellar Populations. *Astrophys. J.* **745**, 50 (2012).
- [4] Jaacks, J., Finkelstein, S. L. & Bromm, V. Legacy of star formation in the pre-reionization universe. *Mon. Not. R. Astron. Soc.* **488**, 2202–2221 (2019).
- [5] Castellano, M. *et al.* Early Results from GLASS-JWST. III. Galaxy Candidates at z 9–15. *Astrophys. J. Lett.* **938**, L15 (2022).
- [6] Naidu, R. P. *et al.* Two Remarkably Luminous Galaxy Candidates at $z \approx 10$ –12 Revealed by JWST. *Astrophys. J. Lett.* **940**, L14 (2022).
- [7] Finkelstein, S. L. *et al.* A Long Time Ago in a Galaxy Far, Far Away: A Candidate $z \sim 12$ Galaxy in Early JWST CEERS Imaging. *Astrophys. J. Lett.* **940**, L55 (2022).
- [8] Donnan, C. T. *et al.* The evolution of the galaxy UV luminosity function at redshifts $z \sim 8$ – 15 from deep JWST and ground-based near-infrared imaging. *Mon. Not. R. Astron. Soc.* **518**, 6011–6040 (2023).
- [9] Adams, N. J. *et al.* Discovery and properties of ultra-high redshift galaxies ($9 < z < 12$) in the JWST ERO SMACS 0723 Field. *Mon. Not. R. Astron. Soc.* **518**, 4755–4766 (2023).
- [10] Harikane, Y. *et al.* A Comprehensive Study of Galaxies at $z \sim 9$ –16 Found in the Early JWST Data: Ultraviolet Luminosity Functions and Cosmic Star Formation History at the Pre-reionization Epoch. *Astrophys. J. Suppl. Ser.* **265**, 5 (2023).
- [11] Atek, H. *et al.* Revealing galaxy candidates out to $z \sim 16$ with JWST observations of the lensing cluster SMACS0723. *Mon. Not. R. Astron. Soc.* **519**, 1201–1220 (2023).
- [12] Finkelstein, S. L. *et al.* CEERS Key Paper I: An Early Look into the First 500 Myr of Galaxy Formation with JWST. *arXiv e-prints* arXiv:2211.05792 (2022).

- [13] Boylan-Kolchin, M. Stress Testing Λ CDM with High-redshift Galaxy Candidates. *arXiv e-prints* arXiv:2208.01611 (2022).
- [14] Rieke, M. J. *et al.* NGST NIRC*am* Scientific Program and Design Concept. In Mather, J. C. (ed.) *IR Space Telescopes and Instruments*, vol. 4850 of *Society of Photo-Optical Instrumentation Engineers (SPIE) Conference Series*, 478–485 (2003).
- [15] Rieke, M. J., Kelly, D. & Horner, S. Overview of James Webb Space Telescope and NIRC*am*'s Role. In Heaney, J. B. & Burriesci, L. G. (eds.) *Cryogenic Optical Systems and Instruments XI*, vol. 5904 of *Society of Photo-Optical Instrumentation Engineers (SPIE) Conference Series*, 1–8 (2005).
- [16] Beichman, C. A. *et al.* Science opportunities with the near-IR camera (NIRC*am*) on the James Webb Space Telescope (JWST). In Clampin, M. C., Fazio, G. G., MacEwen, H. A. & Oschmann, J., Jacobus M. (eds.) *Space Telescopes and Instrumentation 2012: Optical, Infrared, and Millimeter Wave*, vol. 8442 of *Society of Photo-Optical Instrumentation Engineers (SPIE) Conference Series*, 84422N (2012).
- [17] Bagley, M. B. *et al.* CEERS Epoch 1 NIRC*am* Imaging: Reduction Methods and Simulations Enabling Early JWST Science Results. *arXiv e-prints* arXiv:2211.02495 (2022).
- [18] Curtis-Lake, E. *et al.* Spectroscopic confirmation of four metal-poor galaxies at $z=10.3-13.2$. *arXiv e-prints* arXiv:2212.04568 (2022).
- [19] Bouwens, R. *et al.* UV Luminosity Density Results at $z>8$ from the First JWST/NIRC*am* Fields: Limitations of Early Data Sets and the Need for Spectroscopy. *arXiv e-prints* arXiv:2212.06683 (2022).
- [20] Naidu, R. P. *et al.* Schrodinger's Galaxy Candidate: Puzzlingly Luminous at $z \approx 17$, or Dusty/Quenched at $z \approx 5$? *arXiv e-prints* arXiv:2208.02794 (2022).
- [21] Pérez-González, P. G. *et al.* CEERS Key Paper V: A triality on the nature of HST-dark galaxies. *arXiv e-prints* arXiv:2211.00045 (2022).
- [22] Zavala, J. A. *et al.* Dusty Starbursts Masquerading as Ultra-high Redshift Galaxies in JWST CEERS Observations. *Astrophys. J. Lett.* **943**, L9 (2023).
- [23] Jakobsen, P. *et al.* The Near-Infrared Spectrograph (NIRSpec) on the James Webb Space Telescope. I. Overview of the instrument and its capabilities. *Astron. Astrophys.* **661**, A80 (2022).

- [24] Boyett, K. *et al.* A massive interacting galaxy 525 million years after the Big Bang. *arXiv e-prints* arXiv:2303.00306 (2023).
- [25] Fujimoto, S. *et al.* CEERS Spectroscopic Confirmation of NIRCam-Selected $z > 8$ Galaxy Candidates with JWST/NIRSpec: Initial Characterization of their Properties. *arXiv e-prints* arXiv:2301.09482 (2023).
- [26] Trump, J. R. *et al.* The Physical Conditions of Emission-line Galaxies at Cosmic Dawn from JWST/NIRSpec Spectroscopy in the SMACS 0723 Early Release Observations. *Astrophys. J.* **945**, 35 (2023).
- [27] Williams, H. *et al.* A Highly Magnified and Extremely Compact Galaxy at Redshift 9.51 with Strong Nebular Emission. *arXiv e-prints* arXiv:2210.15699 (2022).
- [28] Kocevski, D. D. *et al.* Hidden Little Monsters: Spectroscopic Identification of Low-Mass, Broad-Line AGN at $z > 5$ with CEERS. *arXiv e-prints* arXiv:2302.00012 (2023).
- [29] Larson, R. L. *et al.* A CEERS Discovery of an Accreting Supermassive Black Hole 570 Myr after the Big Bang: Identifying a Progenitor of Massive $z > 6$ Quasars. *arXiv e-prints* arXiv:2303.08918 (2023).
- [30] Bunker, A. J. *et al.* JADES NIRSpec Spectroscopy of GN-z11: Lyman- α emission and possible enhanced nitrogen abundance in a $z = 10.60$ luminous galaxy. *arXiv e-prints* arXiv:2302.07256 (2023).
- [31] Bromm, V., Kudritzki, R. P. & Loeb, A. Generic Spectrum and Ionization Efficiency of a Heavy Initial Mass Function for the First Stars. *Astrophys. J.* **552**, 464–472 (2001).
- [32] Sharda, P. & Krumholz, M. R. When did the initial mass function become bottom-heavy? *Mon. Not. R. Astron. Soc.* **509**, 1959–1984 (2022).
- [33] Larson, R. B. Early star formation and the evolution of the stellar initial mass function in galaxies. *Mon. Not. R. Astron. Soc.* **301**, 569–581 (1998).
- [34] Brammer, G. B., van Dokkum, P. G. & Coppi, P. EAZY: A Fast, Public Photometric Redshift Code. *Astrophys. J.* **686**, 1503–1513 (2008).
- [35] Larson, R. L. *et al.* Spectral Templates Optimal for Selecting Galaxies at $z > 8$ with JWST. *arXiv e-prints* arXiv:2211.10035 (2022).
- [36] CASA Team *et al.* CASA, the Common Astronomy Software Applications for Radio Astronomy. *PASP* **134**, 114501 (2022).
- [37] Ferruit, P. *et al.* The Near-Infrared Spectrograph (NIRSpec) on the James Webb Space Telescope. II. Multi-object spectroscopy (MOS). *Astron.*

- Astrophys.* **661**, A81 (2022).
- [38] Developers, J. *et al.* Jdaviz. Zenodo (2023).
- [39] Arrabal Haro, P. *et al.* TBD. *ApJ Submitted* **TBD**, TBD (2023).
- [40] Storey, P. J., Sochi, T. & Badnell, N. R. Collision strengths for nebular [OIII] optical and infrared lines. *Monthly Notices of the Royal Astronomical Society* **441**, 3028–3039 (2014). URL <https://doi.org/10.1093/mnras/stu777>.
- [41] Dijkstra, M. Ly α Emitting Galaxies as a Probe of Reionisation. *PASA* **31**, 40 (2014).
- [42] Finkelstein, S. L. *et al.* Conditions for Reionizing the Universe with a Low Galaxy Ionizing Photon Escape Fraction. *Astrophys. J.* **879**, 36 (2019).
- [43] Jung, I. *et al.* Evidence for Reduced Specific Star Formation Rates in the Centers of Massive Galaxies at $z = 4$. *Astrophys. J.* **834**, 81 (2017).
- [44] Carnall, A. C., McLure, R. J., Dunlop, J. S. & Davé, R. Inferring the star formation histories of massive quiescent galaxies with BAGPIPES: evidence for multiple quenching mechanisms. *Mon. Not. R. Astron. Soc.* **480**, 4379–4401 (2018).
- [45] Boquien, M. *et al.* CIGALE: a python Code Investigating GALaxy Emission. *Astron. Astrophys.* **622**, A103 (2019).
- [46] Pérez-González, P. G. *et al.* The Stellar Mass Assembly of Galaxies from $z = 0$ to $z = 4$: Analysis of a Sample Selected in the Rest-Frame Near-Infrared with Spitzer. *Astrophys. J.* **675**, 234–261 (2008).
- [47] Carnall, A. C. *et al.* How to Measure Galaxy Star Formation Histories. I. Parametric Models. *Astrophys. J.* **873**, 44 (2019).
- [48] Leja, J., Carnall, A. C., Johnson, B. D., Conroy, C. & Speagle, J. S. How to Measure Galaxy Star Formation Histories. II. Nonparametric Models. *Astrophys. J.* **876**, 3 (2019).
- [49] Pacifici, C. *et al.* The Art of Measuring Physical Parameters in Galaxies: A Critical Assessment of Spectral Energy Distribution Fitting Techniques. *Astrophys. J.* **944**, 141 (2023).
- [50] Bruzual, G. & Charlot, S. Stellar population synthesis at the resolution of 2003. *Mon. Not. R. Astron. Soc.* **344**, 1000–1028 (2003).
- [51] Ferland, G. J. *et al.* The 2017 Release Cloudy. *Rev. Mex. Astron. Astrofis.* **53**, 385–438 (2017).

- [52] Salim, S., Boquien, M. & Lee, J. C. Dust Attenuation Curves in the Local Universe: Demographics and New Laws for Star-forming Galaxies and High-redshift Analogs. *Astrophys. J.* **859**, 11 (2018).
- [53] Carnall, A. C. *et al.* A first look at the SMACS0723 JWST ERO: spectroscopic redshifts, stellar masses, and star-formation histories. *Mon. Not. R. Astron. Soc.* **518**, L45–L50 (2023).
- [54] Burgarella, D., Buat, V. & Iglesias-Páramo, J. Star formation and dust attenuation properties in galaxies from a statistical ultraviolet-to-far-infrared analysis. *Mon. Not. R. Astron. Soc.* **360**, 1413–1425 (2005).
- [55] Boquien, M. *et al.* CIGALE: a python Code Investigating GALaxy Emission. *Astron. Astrophys.* **622**, A103 (2019).
- [56] Calzetti, D. *et al.* The Dust Content and Opacity of Actively Star-forming Galaxies. *Astrophys. J.* **533**, 682–695 (2000).
- [57] Pei, Y. C. Interstellar Dust from the Milky Way to the Magellanic Clouds. *Astrophys. J.* **395**, 130 (1992).
- [58] Bruzual, G. & Charlot, S. Stellar population synthesis at the resolution of 2003. *Mon. Not. R. Astron. Soc.* **344**, 1000–1028 (2003).
- [59] Chabrier, G. Galactic Stellar and Substellar Initial Mass Function. *PASP* **115**, 763–795 (2003).
- [60] Calzetti, D. *et al.* The Dust Content and Opacity of Actively Star-forming Galaxies. *Astrophys. J.* **533**, 682–695 (2000).
- [61] Pérez-González, P. G. *et al.* Stellar populations in local star-forming galaxies - I. Data and modelling procedure. *Mon. Not. R. Astron. Soc.* **338**, 508–524 (2003).
- [62] Fernández, V., Amorín, R., Sanchez-Janssen, R., del Valle-Espinosa, M. G. & Papaderos, P. The resolved chemical composition of the starburst dwarf galaxy CGCG007-025: direct method versus photoionization model fitting. *Monthly Notices of the Royal Astronomical Society* **520**, 3576–3590 (2023). URL <https://doi.org/10.1093/mnras/stad198>.

References

- [1] Bromm, V., Coppi, P. S. & Larson, R. B. The Formation of the First Stars. I. The Primordial Star-forming Cloud. *Astrophys. J.* **564**, 23–51 (2002).

- [2] Schneider, R., Ferrara, A., Natarajan, P. & Omukai, K. First Stars, Very Massive Black Holes, and Metals. *Astrophys. J.* **571**, 30–39 (2002).
- [3] Wise, J. H., Turk, M. J., Norman, M. L. & Abel, T. The Birth of a Galaxy: Primordial Metal Enrichment and Stellar Populations. *Astrophys. J.* **745**, 50 (2012).
- [4] Jaacks, J., Finkelstein, S. L. & Bromm, V. Legacy of star formation in the pre-reionization universe. *Mon. Not. R. Astron. Soc.* **488**, 2202–2221 (2019).
- [5] Castellano, M. *et al.* Early Results from GLASS-JWST. III. Galaxy Candidates at z 9–15. *Astrophys. J. Lett.* **938**, L15 (2022).
- [6] Naidu, R. P. *et al.* Two Remarkably Luminous Galaxy Candidates at $z \approx 10$ –12 Revealed by JWST. *Astrophys. J. Lett.* **940**, L14 (2022).
- [7] Finkelstein, S. L. *et al.* A Long Time Ago in a Galaxy Far, Far Away: A Candidate $z \sim 12$ Galaxy in Early JWST CEERS Imaging. *Astrophys. J. Lett.* **940**, L55 (2022).
- [8] Donnan, C. T. *et al.* The evolution of the galaxy UV luminosity function at redshifts $z \sim 8$ –15 from deep JWST and ground-based near-infrared imaging. *Mon. Not. R. Astron. Soc.* **518**, 6011–6040 (2023).
- [9] Adams, N. J. *et al.* Discovery and properties of ultra-high redshift galaxies ($9 < z < 12$) in the JWST ERO SMACS 0723 Field. *Mon. Not. R. Astron. Soc.* **518**, 4755–4766 (2023).
- [10] Harikane, Y. *et al.* A Comprehensive Study of Galaxies at $z \sim 9$ –16 Found in the Early JWST Data: Ultraviolet Luminosity Functions and Cosmic Star Formation History at the Pre-reionization Epoch. *Astrophys. J. Suppl. Ser.* **265**, 5 (2023).
- [11] Atek, H. *et al.* Revealing galaxy candidates out to $z \sim 16$ with JWST observations of the lensing cluster SMACS0723. *Mon. Not. R. Astron. Soc.* **519**, 1201–1220 (2023).
- [12] Finkelstein, S. L. *et al.* CEERS Key Paper I: An Early Look into the First 500 Myr of Galaxy Formation with JWST. *arXiv e-prints* arXiv:2211.05792 (2022).
- [13] Boylan-Kolchin, M. Stress Testing Λ CDM with High-redshift Galaxy Candidates. *arXiv e-prints* arXiv:2208.01611 (2022).
- [14] Rieke, M. J. *et al.* NGST NIRC*am* Scientific Program and Design Concept. In Mather, J. C. (ed.) *IR Space Telescopes and Instruments*,

- vol. 4850 of *Society of Photo-Optical Instrumentation Engineers (SPIE) Conference Series*, 478–485 (2003).
- [15] Rieke, M. J., Kelly, D. & Horner, S. Overview of James Webb Space Telescope and NIRC*am*'s Role. In Heaney, J. B. & Burriesci, L. G. (eds.) *Cryogenic Optical Systems and Instruments XI*, vol. 5904 of *Society of Photo-Optical Instrumentation Engineers (SPIE) Conference Series*, 1–8 (2005).
- [16] Beichman, C. A. *et al.* Science opportunities with the near-IR camera (NIRC*am*) on the James Webb Space Telescope (JWST). In Clampin, M. C., Fazio, G. G., MacEwen, H. A. & Oschmann, J., Jacobus M. (eds.) *Space Telescopes and Instrumentation 2012: Optical, Infrared, and Millimeter Wave*, vol. 8442 of *Society of Photo-Optical Instrumentation Engineers (SPIE) Conference Series*, 84422N (2012).
- [17] Bagley, M. B. *et al.* CEERS Epoch 1 NIRC*am* Imaging: Reduction Methods and Simulations Enabling Early JWST Science Results. *arXiv e-prints* arXiv:2211.02495 (2022).
- [18] Curtis-Lake, E. *et al.* Spectroscopic confirmation of four metal-poor galaxies at $z=10.3-13.2$. *arXiv e-prints* arXiv:2212.04568 (2022).
- [19] Bouwens, R. *et al.* UV Luminosity Density Results at $z>8$ from the First JWST/NIRC*am* Fields: Limitations of Early Data Sets and the Need for Spectroscopy. *arXiv e-prints* arXiv:2212.06683 (2022).
- [20] Naidu, R. P. *et al.* Schrodinger's Galaxy Candidate: Puzzlingly Luminous at $z \approx 17$, or Dusty/Quenched at $z \approx 5$? *arXiv e-prints* arXiv:2208.02794 (2022).
- [21] Pérez-González, P. G. *et al.* CEERS Key Paper V: A triality on the nature of HST-dark galaxies. *arXiv e-prints* arXiv:2211.00045 (2022).
- [22] Zavala, J. A. *et al.* Dusty Starbursts Masquerading as Ultra-high Redshift Galaxies in JWST CEERS Observations. *Astrophys. J. Lett.* **943**, L9 (2023).
- [23] Jakobsen, P. *et al.* The Near-Infrared Spectrograph (NIRSpec) on the James Webb Space Telescope. I. Overview of the instrument and its capabilities. *Astron. Astrophys.* **661**, A80 (2022).
- [24] Boyett, K. *et al.* A massive interacting galaxy 525 million years after the Big Bang. *arXiv e-prints* arXiv:2303.00306 (2023).

- [25] Fujimoto, S. *et al.* CEERS Spectroscopic Confirmation of NIRCam-Selected $z > 8$ Galaxy Candidates with JWST/NIRSpec: Initial Characterization of their Properties. *arXiv e-prints* arXiv:2301.09482 (2023).
- [26] Trump, J. R. *et al.* The Physical Conditions of Emission-line Galaxies at Cosmic Dawn from JWST/NIRSpec Spectroscopy in the SMACS 0723 Early Release Observations. *Astrophys. J.* **945**, 35 (2023).
- [27] Williams, H. *et al.* A Highly Magnified and Extremely Compact Galaxy at Redshift 9.51 with Strong Nebular Emission. *arXiv e-prints* arXiv:2210.15699 (2022).
- [28] Kocevski, D. D. *et al.* Hidden Little Monsters: Spectroscopic Identification of Low-Mass, Broad-Line AGN at $z > 5$ with CEERS. *arXiv e-prints* arXiv:2302.00012 (2023).
- [29] Larson, R. L. *et al.* A CEERS Discovery of an Accreting Supermassive Black Hole 570 Myr after the Big Bang: Identifying a Progenitor of Massive $z > 6$ Quasars. *arXiv e-prints* arXiv:2303.08918 (2023).
- [30] Bunker, A. J. *et al.* JADES NIRSpec Spectroscopy of GN-z11: Lyman- α emission and possible enhanced nitrogen abundance in a $z = 10.60$ luminous galaxy. *arXiv e-prints* arXiv:2302.07256 (2023).
- [31] Bromm, V., Kudritzki, R. P. & Loeb, A. Generic Spectrum and Ionization Efficiency of a Heavy Initial Mass Function for the First Stars. *Astrophys. J.* **552**, 464–472 (2001).
- [32] Sharda, P. & Krumholz, M. R. When did the initial mass function become bottom-heavy? *Mon. Not. R. Astron. Soc.* **509**, 1959–1984 (2022).
- [33] Larson, R. B. Early star formation and the evolution of the stellar initial mass function in galaxies. *Mon. Not. R. Astron. Soc.* **301**, 569–581 (1998).
- [34] Brammer, G. B., van Dokkum, P. G. & Coppi, P. EAZY: A Fast, Public Photometric Redshift Code. *Astrophys. J.* **686**, 1503–1513 (2008).
- [35] Larson, R. L. *et al.* Spectral Templates Optimal for Selecting Galaxies at $z > 8$ with JWST. *arXiv e-prints* arXiv:2211.10035 (2022).
- [36] CASA Team *et al.* CASA, the Common Astronomy Software Applications for Radio Astronomy. *PASP* **134**, 114501 (2022).
- [37] Ferruit, P. *et al.* The Near-Infrared Spectrograph (NIRSpec) on the James Webb Space Telescope. II. Multi-object spectroscopy (MOS). *Astron. Astrophys.* **661**, A81 (2022).
- [38] Developers, J. *et al.* Jdaviz. Zenodo (2023).

- [39] Arrabal Haro, P. *et al.* TBD. *ApJ Submitted* **TBD**, TBD (2023).
- [40] Storey, P. J., Sochi, T. & Badnell, N. R. Collision strengths for nebular [OIII] optical and infrared lines. *Monthly Notices of the Royal Astronomical Society* **441**, 3028–3039 (2014). URL <https://doi.org/10.1093/mnras/stu777>.
- [41] Dijkstra, M. Ly α Emitting Galaxies as a Probe of Reionisation. *PASA* **31**, 40 (2014).
- [42] Finkelstein, S. L. *et al.* Conditions for Reionizing the Universe with a Low Galaxy Ionizing Photon Escape Fraction. *Astrophys. J.* **879**, 36 (2019).
- [43] Jung, I. *et al.* Evidence for Reduced Specific Star Formation Rates in the Centers of Massive Galaxies at $z = 4$. *Astrophys. J.* **834**, 81 (2017).
- [44] Carnall, A. C., McLure, R. J., Dunlop, J. S. & Davé, R. Inferring the star formation histories of massive quiescent galaxies with BAGPIPES: evidence for multiple quenching mechanisms. *Mon. Not. R. Astron. Soc.* **480**, 4379–4401 (2018).
- [45] Boquien, M. *et al.* CIGALE: a python Code Investigating GALaxy Emission. *Astron. Astrophys.* **622**, A103 (2019).
- [46] Pérez-González, P. G. *et al.* The Stellar Mass Assembly of Galaxies from $z = 0$ to $z = 4$: Analysis of a Sample Selected in the Rest-Frame Near-Infrared with Spitzer. *Astrophys. J.* **675**, 234–261 (2008).
- [47] Carnall, A. C. *et al.* How to Measure Galaxy Star Formation Histories. I. Parametric Models. *Astrophys. J.* **873**, 44 (2019).
- [48] Leja, J., Carnall, A. C., Johnson, B. D., Conroy, C. & Speagle, J. S. How to Measure Galaxy Star Formation Histories. II. Nonparametric Models. *Astrophys. J.* **876**, 3 (2019).
- [49] Pacifici, C. *et al.* The Art of Measuring Physical Parameters in Galaxies: A Critical Assessment of Spectral Energy Distribution Fitting Techniques. *Astrophys. J.* **944**, 141 (2023).
- [50] Bruzual, G. & Charlot, S. Stellar population synthesis at the resolution of 2003. *Mon. Not. R. Astron. Soc.* **344**, 1000–1028 (2003).
- [51] Ferland, G. J. *et al.* The 2017 Release Cloudy. *Rev. Mex. Astron. Astrofis.* **53**, 385–438 (2017).
- [52] Salim, S., Boquien, M. & Lee, J. C. Dust Attenuation Curves in the Local Universe: Demographics and New Laws for Star-forming Galaxies and High-redshift Analogs. *Astrophys. J.* **859**, 11 (2018).

- [53] Carnall, A. C. *et al.* A first look at the SMACS0723 JWST ERO: spectroscopic redshifts, stellar masses, and star-formation histories. *Mon. Not. R. Astron. Soc.* **518**, L45–L50 (2023).
- [54] Burgarella, D., Buat, V. & Iglesias-Páramo, J. Star formation and dust attenuation properties in galaxies from a statistical ultraviolet-to-far-infrared analysis. *Mon. Not. R. Astron. Soc.* **360**, 1413–1425 (2005).
- [55] Boquien, M. *et al.* CIGALE: a python Code Investigating GALaxy Emission. *Astron. Astrophys.* **622**, A103 (2019).
- [56] Calzetti, D. *et al.* The Dust Content and Opacity of Actively Star-forming Galaxies. *Astrophys. J.* **533**, 682–695 (2000).
- [57] Pei, Y. C. Interstellar Dust from the Milky Way to the Magellanic Clouds. *Astrophys. J.* **395**, 130 (1992).
- [58] Bruzual, G. & Charlot, S. Stellar population synthesis at the resolution of 2003. *Mon. Not. R. Astron. Soc.* **344**, 1000–1028 (2003).
- [59] Chabrier, G. Galactic Stellar and Substellar Initial Mass Function. *PASP* **115**, 763–795 (2003).
- [60] Calzetti, D. *et al.* The Dust Content and Opacity of Actively Star-forming Galaxies. *Astrophys. J.* **533**, 682–695 (2000).
- [61] Pérez-González, P. G. *et al.* Stellar populations in local star-forming galaxies - I. Data and modelling procedure. *Mon. Not. R. Astron. Soc.* **338**, 508–524 (2003).
- [62] Fernández, V., Amorín, R., Sanchez-Janssen, R., del Valle-Espinosa, M. G. & Papaderos, P. The resolved chemical composition of the starburst dwarf galaxy CGCG007-025: direct method versus photoionization model fitting. *Monthly Notices of the Royal Astronomical Society* **520**, 3576–3590 (2023). URL <https://doi.org/10.1093/mnras/stad198>.